Progress of Theoretical Physics, Vol. 113, No. 6, June 2005

Comparative Study of Octupole Excitations on Superdeformed States in ^{32}S, ^{36}S, ^{40}Ca and ^{50}S

Kenichi YOSHIDA,[1] Masayuki YAMAGAMI[2] and Kenichi MATSUYANAGI[1]

[1]*Department of Physics, Graduate School of Science, Kyoto University, Kyoto 606-8502, Japan*
[2]*Heavy Ion Nuclear Physics Laboratory, RIKEN, Wako 351-0198, Japan*

(Received January 27, 2005)

By means of an RPA calculation based on the deformed Woods-Saxon potential in the coordinate-mesh representation, we make a comparative study of octupole excitations built on superdeformed states in the ^{40}Ca region and those in ^{50}S. For the $N = Z$ stable nuclei, ^{32}S and ^{40}Ca, enhancement of octupole transition strengths results from the coherence of the proton and neutron excitations. Contrastingly, for ^{50}S close to the neutron drip line, we find that the low-lying state created by the excitation of a single neutron from a loosely bound low Ω state to a high Ω resonance state acquires an extremely large transition strength. A similar enhancement of the octupole strength is also found in oblately deformed ^{40}Mg close to the neutron drip line.

§1. Introduction

In recent years, the physics of unstable nuclei close to the drip line has become one of the most active fields in nuclear structure physics. New features, such as neutron skins and shell structure near the continuum, are currently being actively investigated both theoretically and experimentally.[1)–3)] Although, at present, drip-line nuclei that allow for relevant experiments are largely restricted to light nuclei, the region of unstable nuclei that can be explored experimentally will soon be significantly extended to medium-mass regions, when new facilities for radioactive ion beams start running. To investigate the possibility of the emergence of excitation modes unique to unstable nuclei in heavier-mass regions, many attempts have been made using the self-consistent RPA based on the Skyrme-Hartree-Fock (SHF) method[4)–6)] and its extensions, including pairing correlations.[7)–10)] A number of similar approaches using different mean fields have also been employed.[11)–14)] (See Refs. 10) and 15) for extensive lists of references concerning the self-consistent RPA and mean-field theories.) To describe such weakly bound systems for which the Fermi energy is close to zero, it is essential to properly treat the particle-hole excitations into the continuum. Thus, the continuum RPA method employing the Green functions that satisfy the scattering boundary condition has been widely used.[4)–7),16),17)] Quite recently, this method was extended to the continuum quasiparticle-RPA, taking into account pairing correlations.[18)–22)] However, most of these investigations are restricted to spherical nuclei. For deformed unstable nuclei, although low-lying Gamow-Teller β-decay strengths have been investigated[23)] by means of the standard matrix formulation of the RPA, other low-frequency RPA modes remain largely unexplored, except some recent attempts to describe low-frequency isovector dipole modes using

the time-dependent Hartree-Fock method with absorbing boundary conditions[24),25)] and gamma vibrations using the quasiparticle-RPA with the BCS approximation.[26)]

In order to clearly see the deformation effects in unstable nuclei, Inakura et al.[27),28)] investigated properties of negative-parity collective excitations built on superdeformed (SD) states in neutron-rich sulfur isotopes by means of the mixed representation RPA[29)–32)] based on the SHF mean field, and found many low-energy modes possessing strongly enhanced isoscalar octupole transition strengths. They also studied excitation modes built on the SD states in the ^{40}Ca region with $N = Z$, for which the SD yrast states have been discovered in recent experiments.[33),34)] In the mixed representation RPA, the *particle* states are treated using the coordinate-mesh representation, while the HF basis is used for the *hole* states. This approach is fully self-consistent in that the same effective interaction is used in both the mean-field and RPA calculations. Also, it is unnecessary to introduce an upper cutoff with respect to the energies of the *particle* states. On the other hand, it is not easy in this method to identify microscopic particle-hole configurations generating individual RPA modes. Therefore, using the deformed Woods-Saxon potential and the conventional matrix formulation of the RPA, we have made a detailed analysis of the microscopic structure of octupole excitation modes built on the SD states in the ^{40}Ca region with $N = Z$ and the ^{50}S region close to the neutron drip line. In this approach, we can easily obtain a simple and transparent understanding of the particle-hole configurations generating the RPA eigenmodes.

This paper is organized as follows. In the next section, the frameworks of the mean-field and RPA calculations are described. In §3.1, the results of the RPA calculation for the SD states in ^{32}S, ^{36}S and ^{40}Ca are presented and discussed. In §3.2, we present the result for ^{50}S close to the neutron drip line and suggest that some low-lying states associated with excitations of a single neutron from a loosely bound state to a resonance state acquire extremely strong transition strengths. In §3.3, we discuss excitation modes in the oblately deformed ^{40}Mg and suggest that the results obtained for ^{50}S are not restricted to the SD states but are rather general phenomena. Conclusions are given in §4.

§2. Method of calculation

2.1. *Mean-field calculation*

We consider the single-particle motion in an axially symmetric deformed potential. Using the standard notation, the Schrödinger equation is written

$$\left\{-\frac{\hbar^2}{2m}\nabla^2 + V_{WS}f(\boldsymbol{r}) + V_{SO}\nabla f(\boldsymbol{r})\cdot(\boldsymbol{\sigma}\times\boldsymbol{p}) + V_C(\boldsymbol{r})\frac{(1-\tau_3)}{2}\right\}\Phi_i = e_i\Phi_i. \quad (2\cdot1)$$

The solutions to this equation take the following form:

$$\Phi_i(x) = \Phi_i(\boldsymbol{r},\sigma,\tau) = \chi_{q_i}(\tau)\left[\phi_i^+(\rho,z)e^{i\Lambda_i^-\varphi}\chi_{\frac{1}{2}}(\sigma) + \phi_i^-(\rho,z)e^{i\Lambda_i^+\varphi}\chi_{-\frac{1}{2}}(\sigma)\right]. \quad (2\cdot2)$$

Here, $\Lambda_i^\pm = \Omega_i \pm 1/2$, where Λ_i and Ω_i are the z-components of the total and orbital angular momenta, respectively, and (ρ, z, φ) are the cylindrical coordinates

of $\boldsymbol{r} = (x, y, z)$:

$$x = \rho\cos\varphi, \quad y = \rho\sin\varphi, \quad z = z. \tag{2·3}$$

The subscript $q_i = +1/2$ $(-1/2)$ denotes neutrons (protons). In terms of the wave functions given in (2·2), the nucleon density is given by

$$\varrho(\rho, z) = \sum_i [|\phi_i^+(\rho, z)|^2 + |\phi_i^-(\rho, z)|^2], \tag{2·4}$$

and the mean-square radii of protons and neutrons are calculated as

$$\langle r^2\rangle_\tau = \frac{\int \rho d\rho dz r^2 \varrho_\tau(\rho, z)}{\int \rho d\rho dz \varrho_\tau(\rho, z)}, \tag{2·5}$$

where $r = \sqrt{\rho^2 + z^2}$ and $\tau{=}\pi$ or ν, with $\varrho_\pi(\rho, z)$ and $\varrho_\nu(\rho, z)$ being the proton and neutron densities.

We employ the phenomenological Woods-Saxon potential

$$f(\boldsymbol{r}) = (1 + \exp[(r - R(\theta))/a])^{-1}, \tag{2·6}$$

$$R(\theta) = c(1 + \beta_2 Y_{20}(\theta)), \tag{2·7}$$

where c is determined by the volume conservation condition. Though an angle dependent diffuseness parameter $a(\theta)$ is better for a more accurate calculation,[35] we use a constant $a = 0.67$ fm for simplicity. We also use the standard parameter values[36] for the central and spin-orbit potentials,

$$V_{WS} = -51 + 33\frac{N - Z}{A}\tau_3, \tag{2·8}$$

$$V_{SO} = \frac{1}{2}r_0^2\left(-22 + 14\frac{N - Z}{A}\tau_3\right), \tag{2·9}$$

with $r_0 = 1.27$ fm. The spin-orbit term is written

$$\hat{V}_{ls} = -\frac{1}{2}V_{SO}\left[\sigma_+ e^{-i\varphi}\left\{\frac{\partial f}{\partial\rho}\frac{\partial}{\partial z} - \frac{\partial f}{\partial z}\left(\frac{\partial}{\partial\rho} + \frac{\hat{l_z}}{\rho}\right)\right\}\right.$$
$$\left. + \sigma_- e^{i\varphi}\left\{-\frac{\partial f}{\partial\rho}\frac{\partial}{\partial z} + \frac{\partial f}{\partial z}\left(\frac{\partial}{\partial\rho} - \frac{\hat{l_z}}{\rho}\right)\right\} + \sigma_z 2\frac{\partial f}{\partial\rho}\frac{\hat{l_z}}{\rho}\right], \tag{2·10}$$

where $\sigma_\pm = \sigma_x \pm i\sigma_y$ and $\hat{l}_z = -i\partial/\partial\varphi$. For protons, we solve the Poisson equation, $\nabla^2 V_C(\boldsymbol{r}) = 4\pi e\varrho_\pi(\boldsymbol{r})$, to obtain the Coulomb potential V_C. In the present calculation, we approximate the proton density $\varrho_\pi(\boldsymbol{r})$ by a Woods-Saxon form.

We can rewrite the Schrödinger equation (2·1) in the matrix form

$$h\boldsymbol{\phi} = \begin{pmatrix} h_{\uparrow\uparrow} & h_{\uparrow\downarrow} \\ h_{\downarrow\uparrow} & h_{\downarrow\downarrow} \end{pmatrix}\begin{pmatrix} \phi_i^+(\rho, z) \\ \phi_i^-(\rho, z) \end{pmatrix} = e_i \begin{pmatrix} \phi_i^+(\rho, z) \\ \phi_i^-(\rho, z) \end{pmatrix}, \tag{2·11}$$

where

$$h_{\uparrow\uparrow} = -\frac{\hbar^2}{2m}\left[\frac{\partial^2}{\partial\rho^2} + \frac{1}{\rho}\frac{\partial}{\partial\rho} + \frac{\partial^2}{\partial z^2} - \left(\frac{\Lambda^-}{\rho}\right)^2\right] + V_{WS}f(\rho,z) - V_{SO}\frac{\partial f(\rho,z)}{\partial\rho}\frac{\Lambda^-}{\rho}, \tag{2·12a}$$

$$h_{\downarrow\downarrow} = -\frac{\hbar^2}{2m}\left[\frac{\partial^2}{\partial\rho^2} + \frac{1}{\rho}\frac{\partial}{\partial\rho} + \frac{\partial^2}{\partial z^2} - \left(\frac{\Lambda^+}{\rho}\right)^2\right] + V_{WS}f(\rho,z) + V_{SO}\frac{\partial f(\rho,z)}{\partial\rho}\frac{\Lambda^+}{\rho}, \tag{2·12b}$$

$$h_{\uparrow\downarrow} = -\frac{1}{2}V_{SO}\left[\frac{\partial f(\rho,z)}{\partial\rho}\frac{\partial}{\partial z} - \frac{\partial f(\rho,z)}{\partial z}\left(\frac{\partial}{\partial\rho} + \frac{\Lambda^+}{\rho}\right)\right], \tag{2·12c}$$

$$h_{\downarrow\uparrow} = -\frac{1}{2}V_{SO}\left[-\frac{\partial f(\rho,z)}{\partial\rho}\frac{\partial}{\partial z} + \frac{\partial f(\rho,z)}{\partial z}\left(\frac{\partial}{\partial\rho} - \frac{\Lambda^-}{\rho}\right)\right]. \tag{2·12d}$$

Because this equation possesses time-reversal symmetry, we know that if $\Phi_i = \{\phi_i^+, \phi_i^-, \Omega_i\}$ is a solution, then $\Phi_{\bar{i}} = \{-\phi_i^-, \phi_i^+, -\Omega_i\}$ is also a solution with the same eigenvalue e_i, and thus it is sufficient to solve it for positive Ω only. We also assume reflection symmetry with respect to the x-y plane. Then, the wave function $\phi^\pm$ possesses z-parity $\pi(-1)^{\Lambda^\mp}$ as a good quantum number (π being the parity), and therefore it is sufficient to consider only positive z.

We solve Eq. (2·11) directly in coordinate space. In comparison to the conventional method of using a deformed harmonic oscillator basis,[37] this method is believed to be more effective in the treatment of spatially extended wave functions, like loosely bound states, resonant states and continuum states. The Hamiltonian matrix (2·11) is discretized by use of a coordinate mesh in the (ρ, z) plane. The mesh points are chosen as

$$\rho_i = \left(i - \frac{1}{2}\right)\Delta, \qquad i = 1, 2, \cdots N, \tag{2·13}$$

to avoid division by zero, where Δ represents the lattice mesh size. The mesh points in the z direction are taken as

$$z_j = (j-1)\Delta, \qquad j = 1, 2, \cdots M. \tag{2·14}$$

The boundary conditions are set as

$$\phi_{i,M} = \phi_{N,j} = 0, \tag{2·15}$$

where $\phi_{i,j} = \phi(\rho, z)$. We construct the discretized Hamiltonian matrix by use of the finite difference method for derivatives and then diagonalize the matrix to obtain the single-particle wave functions on the two-dimensional lattice. The kinetic energy term is evaluated using the 9-points formula; its explicit expression is given in Appendix A.

2.2. *RPA calculation*

Using the single-particle basis obtained in the previous subsection, we solve the RPA equation in the standard matrix formulation,[38]

$$\sum_{p'h'} \begin{pmatrix} A_{php'h'} & B_{php'h'} \\ B^*_{php'h'} & A^*_{php'h'} \end{pmatrix} \begin{pmatrix} f^\lambda_{p'h'} \\ g^\lambda_{p'h'} \end{pmatrix} = \hbar\omega_\lambda \begin{pmatrix} 1 & 0 \\ 0 & -1 \end{pmatrix} \begin{pmatrix} f^\lambda_{ph} \\ g^\lambda_{ph} \end{pmatrix}, \tag{2·16}$$

where

$$A_{php'h'} = (e_p - e_h)\delta_{pp'}\delta_{hh'} + \bar{v}_{ph'hp'}, \qquad B_{php'h'} = \bar{v}_{pp'hh'}. \tag{2·17}$$

Here, the subscripts p and h denote the single-particle states above and below the Fermi energy (particles and holes), respectively. The antisymmetrized matrix elements of the residual interaction v are denoted $\bar{v}_{ph'hp'}$ and $\bar{v}_{pp'hh'}$. For v, we employ the Skyrme-type interaction[16] without momentum-dependent terms,

$$v(\boldsymbol{r}, \boldsymbol{r}') = \Big[t_0(1 + x_0P_\sigma) + \frac{1}{6}t_3(1 + x_3P_\sigma)\varrho(\boldsymbol{r})\Big]\delta(\boldsymbol{r} - \boldsymbol{r}'), \tag{2·18}$$

with $t_0 = -1100$ MeV·fm^3, $t_3 = 16000$ MeV·fm^6, $x_0 = 0.5$, and $x_3 = 1.0$, P_σ being the spin exchange operator. Because our calculation is not self-consistent in the sense that the residual interaction is not related to the mean-field potential, we renormalize the residual interaction by multiplying it by a factor f to obtain the spurious modes at zero excitation energy: $v \to f \cdot v$.

The intrinsic matrix elements $\langle 0|Q_{3K}|\lambda\rangle$ of the octupole operator Q_{3K} between the excited state $|\lambda\rangle$ and the ground state $|0\rangle$ are given by

$$\langle 0|Q_{3K}|\lambda\rangle = \sum_{ph}\Big(Q^{hp}_{3K}f^\lambda_{ph} + Q^{ph}_{3K}g^\lambda_{ph}\Big) = \sum_{ph} M^{ph}_{3K}, \tag{2·19}$$

and

$$Q^{ph}_{3K} = 2\pi\delta_{K,\Omega_p-\Omega_h}\int\rho d\rho dz\Big(\phi^+_p(\rho,z)\phi^+_h(\rho,z) + \phi^-_p(\rho,z)\phi^-_h(\rho,z)\Big)Q_{3K}(\rho,z) \tag{2·20}$$

$$\equiv 2\pi\delta_{K,\Omega_p-\Omega_h}\int d\rho dz Q^{ph}_{3K}(\rho,z), \tag{2·21}$$

where $Q_{3K}(\rho,z) = Q_{3K}(\boldsymbol{r})e^{-iK\varphi} = r^3Y_{3K}(\theta,\varphi)e^{-iK\varphi}$.

The isoscalar octupole strength function is

$$S^{\rm IS}(\omega) = \sum_\lambda |\langle 0|Q^{\rm IS}_{3K}|\lambda\rangle|^2\delta(\hbar\omega - \hbar\omega_\lambda), \tag{2·22}$$

where $Q^{\rm IS}_{3K} = Q^\pi_{3K} + Q^\nu_{3K}$, and Q^π_{3K} and Q^ν_{3K} are the proton and neutron octupole operators. The reduced isoscalar octupole transition probability is defined by $B(Q^{\rm IS}3) = |\langle 0|Q^{\rm IS}_{3K}|\lambda\rangle|^2$. The reduced proton and neutron octupole transition probabilities, $B(E3)$ and $B(Q^\nu 3)$, are obtained by replacing $Q^{\rm IS}_{3K}$ with eQ^π_{3K} and Q^ν_{3K}, respectively. Note that these quantities represent intrinsic transition strengths, and hence the appropriate Clebsh-Gordan coefficients should be multiplied to obtain transition probabilities in the laboratory frame.

2.3. *Details of numerical calculation*

We numerically solved the Schrödinger equation (2·11) in a rectangular box, using a lattice mesh size $\Delta = 0.5$ fm. The size of the box used was 2.5 (3.5) times the half density radii in the directions of the major and minor axes for ^{32,36}S and ^{40}Ca (^{50}S). Bode's rule was used for the numerical integrations of the RPA matrix elements (see Appendix B). The deformation parameters β_2 were determined so as to approximately reproduce the shell structure near the Fermi level obtained in the SHF calculation by Inakura et al.[39] Their values for protons and neutrons are not necessarily the same. The actual values of the box size used in the calculations are indicated in the figure captions for individual cases, together with the β_2 values adopted. The RPA matrix (2·17) was diagonalized with the cutoff at 30 MeV for the particle-hole excitation energy. In spherical systems, there is only one spurious $J^\pi = 1^-$ mode associated with the center-of-mass motion. In deformed systems, this mode splits into the $K^\pi = 0^-$ and 1^- modes. We find that, e.g., for ^{32}S, the factors $f_0 = 0.7545$ and $f_1 = 0.7723$ are needed to obtain the spurious $K^\pi = 0^-$ and $K^\pi = 1^-$ modes at zero energy. Using these f_0 and f_1 values, we obtain low-lying $K^\pi = 2^-$ states at 2.653 and 2.557 MeV, respectively. This difference of about 0.1 MeV indicates the magnitude of the numerical uncertainty caused by ignoring self-consistency in our calculation. In the following, we choose the factor f such that the excitation energy of the spurious $K^\pi = 1^-$ mode becomes zero.

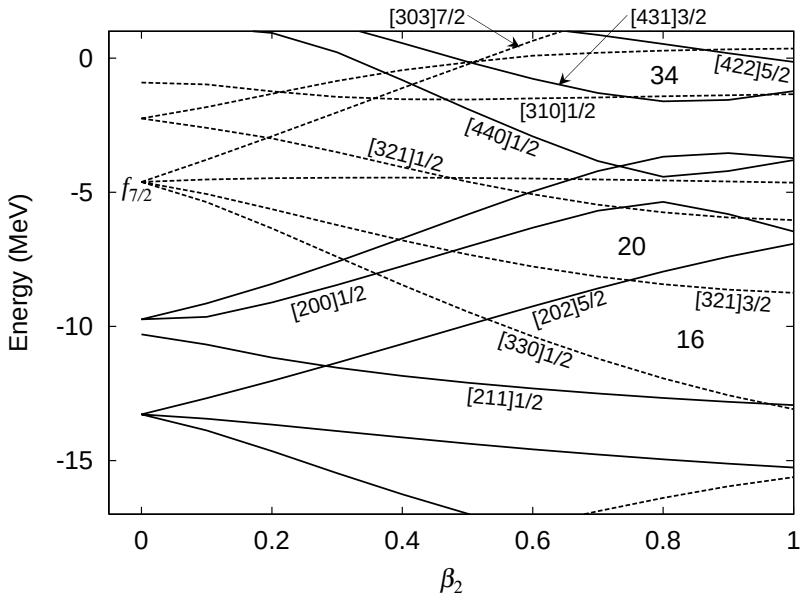

Fig. 1. Neutron single-particle levels in the deformed Woods-Saxon potential, plotted as functions of the quadrupole deformation parameter β_2. The solid and dotted curves denote positive- and negative-parity levels, respectively. The SD magic numbers are $N = 16$, 20 and 34. They are responsible for the appearance of the SD states in ^{32}S, ^{36}S, ^{40}Ca and ^{50}S.

§3. Results and discussion

3.1. *The SD states in ^{32}S, ^{36}S and ^{40}Ca*

We first discuss the result of the RPA calculation for the SD state in ^{32}S. Although the existence of the SD band in ^{32}S has been conjectured for a long time,[40] it has not yet been observed, and this remains a great challenge: As discussed in Refs. 41)–45), the SD local minimum in ^{32}S corresponds to the doubly closed shell configuration with respect to the SD magic number $Z = N = 16$. It involves two protons and two neutrons in the down-sloping single-particle levels originating from the $f_{7/2}$ shell (see Fig. 1). The calculated octupole transition strengths with $K^\pi = 2^-$ are displayed in Fig. 2. A prominent peak is seen at about 2.6 MeV with a strongly enhanced transition strength of about 23 Weisskopf units (1 W.u. $\simeq$ 61 fm^6 for ^{32}S). There are no peaks representing strengths greater than 1 W.u. for other values of K in this energy region. As shown in Table I, the major component of this RPA mode is the particle-hole excitation from the [211]1/2 state to the [321]3/2 state. The proton and neutron excitations act coherently. Other particle-hole configurations also contribute coherently. Here we note that, although the RPA amplitude f_{ph} for the particle-hole excitation from the [330]1/2 state to the [202]5/2 state is appreciable, its contribution to the transition matrix element M_{32}^{ph} is very small. This can be understood from the asymptotic selection rules[47] for low-energy octupole transitions in the SD harmonic-oscillator potential with the axis ratio 2:1:

$$Q_{30}: \quad \Delta N_{\rm sh} = 1,\ \Delta n_3 = 1,\ \Delta\Lambda = 0, \tag{3·1a}$$

$$Q_{31}: \quad \Delta N_{\rm sh} = 0,\ \Delta n_3 = 2,\ \Delta\Lambda = 1, \tag{3·1b}$$

$$Q_{32}: \quad \Delta N_{\rm sh} = 1,\ \Delta n_3 = 1,\ \Delta\Lambda = 2, \tag{3·1c}$$

$$Q_{33}: \quad \Delta N_{\rm sh} = 2,\ \Delta n_3 = 0,\ \Delta\Lambda = 3. \tag{3·1d}$$

Here, the shell quantum number is defined as $N_{\rm sh} = 2n_\perp + n_3$. These selection rules hold approximately also for the SD Wood-Saxon potential under consideration. Accordingly, the [330]1/2 $\rightarrow$ [202]5/2 octupole matrix element is very small, while that of the [211]1/2 $\rightarrow$ [321]3/2 excitation is large. Thus, the coherent proton and neutron excitations from the [211]1/2 hole state to the [321]3/2 particle state are the major origin of the large octupole transition strength for this RPA mode.

Next, let us discuss the result of the RPA calculation for the SD state in ^{40}Ca. As mentioned in §1, for this nucleus, the SD yrast band has been discovered in recent experiments.[33),34)] The SD shell gap at $Z = N = 20$ is associated with the $4p$-$4h$ excitation (for both protons and neutrons) from below the spherical closed shell to the $f_{7/2}$ shell. Figure 3 presents the calculated octupole transition strengths with $K^\pi = 1^-$. It is seen that there are no peaks representing strengths greater than 1.5 W.u. for other values of K in this energy region. There is a prominent peak at 2.2 MeV with an isoscalar strength of about 6 W.u. (1 W.u. $\simeq$ 95 fm^6 for ^{40}Ca). As shown in Table II, this RPA eigenstate consists of components from the coherent proton and neutron excitations from [321]3/2 to [200]1/2, which satisfy the asymptotic selection rule (3·1b).

The SD states in ^{32}S and ^{40}Ca are associated with the SD magic numbers $N =$

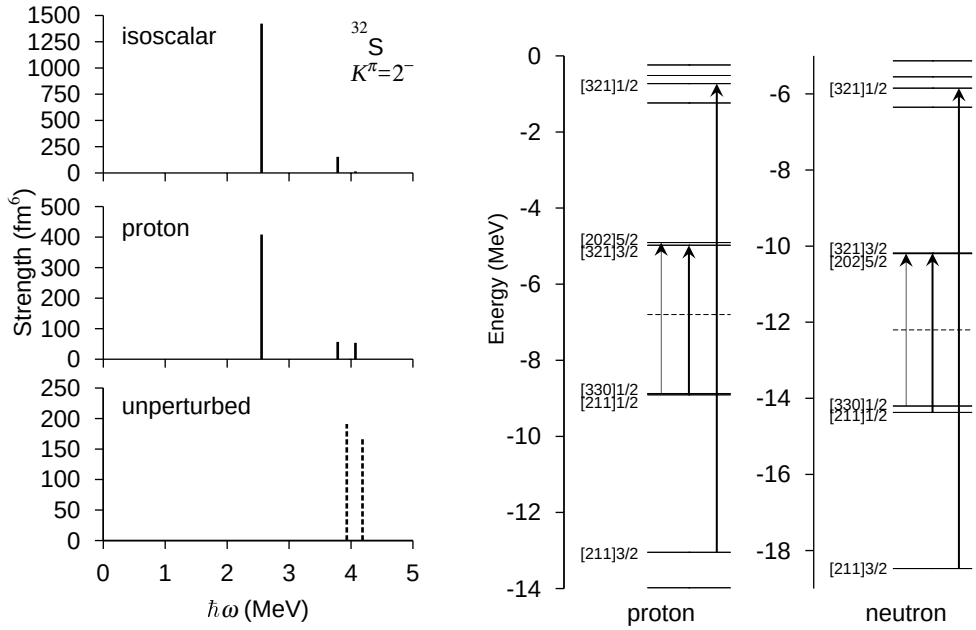

Fig. 2. *Left*: The isoscalar and proton octupole strengths, $B(Q^{\rm IS}3)$ and $B(E3)/e^2$, for the $K^\pi = 2^-$ excitations on the SD state in ^{32}S are plotted in the top and middle panels as functions of the excitation energy. These were obtained using an RPA calculation with $\beta_2 = 0.78$ for both protons and neutrons, using a box of size $\rho_{\max} \times z_{\max} = 8.25$ fm $\times 14.0$ fm. The unperturbed particle-hole strengths are also plotted with dashed lines in the bottom panel. *Right*: Particle-hole configurations generating the lowest $K^\pi = 2^-$ state at 2.6 MeV. Excitations satisfying the asymptotic selection rule Eq. (3·1) are indicated by thick arrows. The asymptotic quantum numbers $[Nn_3\Lambda]\Omega$ are displayed for pertinent levels. The Fermi surfaces for protons and neutrons are indicated by the dashed lines.

Table I. RPA amplitudes for the 2^- state at 2.6 MeV in ^{32}S, calculated with $\beta_2 = 0.78$ for both protons and neutrons. It is characterized by $B(E3) = 408\ e^2$fm^6, $B(Q^\nu 3) = 306$ fm^6, $B(Q^{\rm IS}3) = 1422$ fm^6, and $\sum |g_{ph}|^2 = 1.86 \times 10^{-1}$. The single-particle levels are labeled with the asymptotic quantum numbers $[Nn_3\Lambda]\Omega$. Only components with $|f_{ph}| > 0.1$ are listed.

particle	hole	$\epsilon_p - \epsilon_h$(MeV)	f_{ph}	Q_{32}^{ph} (fm^3)	M_{32}^{ph} (fm^3)
ν[202]5/2	ν[330]1/2	4.01	−0.293	−0.101	0.040
ν[321]3/2	ν[211]1/2	4.19	−0.631	−13.0	11.5
ν[321]1/2	ν[211]3/2	12.6	−0.141	−11.2	2.27
π[202]5/2	π[330]1/2	3.97	−0.282	−0.248	0.096
π[321]3/2	π[211]1/2	3.93	−0.733	−13.8	13.7
π[321]1/2	π[211]3/2	12.3	−0.138	−11.8	2.35

Table II. RPA amplitudes for the 1^- state at 2.2 MeV in ^{40}Ca, calculated with $\beta_2 = 0.6$ for both protons and neutrons. It is characterized by $B(E3) = 122\ e^2$fm^6, $B(Q^\nu 3) = 153$ fm^6, $B(Q^{\rm IS}3) = 549$ fm^6, and $\sum |g_{ph}|^2 = 4.69 \times 10^{-2}$. Only components with $|f_{ph}| > 0.1$ are listed.

particle	hole	$\epsilon_p - \epsilon_h$(MeV)	f_{ph}	Q_{31}^{ph} (fm^3)	M_{31}^{ph} (fm^3)
ν[200]1/2	ν[321]3/2	2.46	0.836	9.08	8.87
π[200]1/2	π[321]3/2	2.59	0.568	10.1	7.06

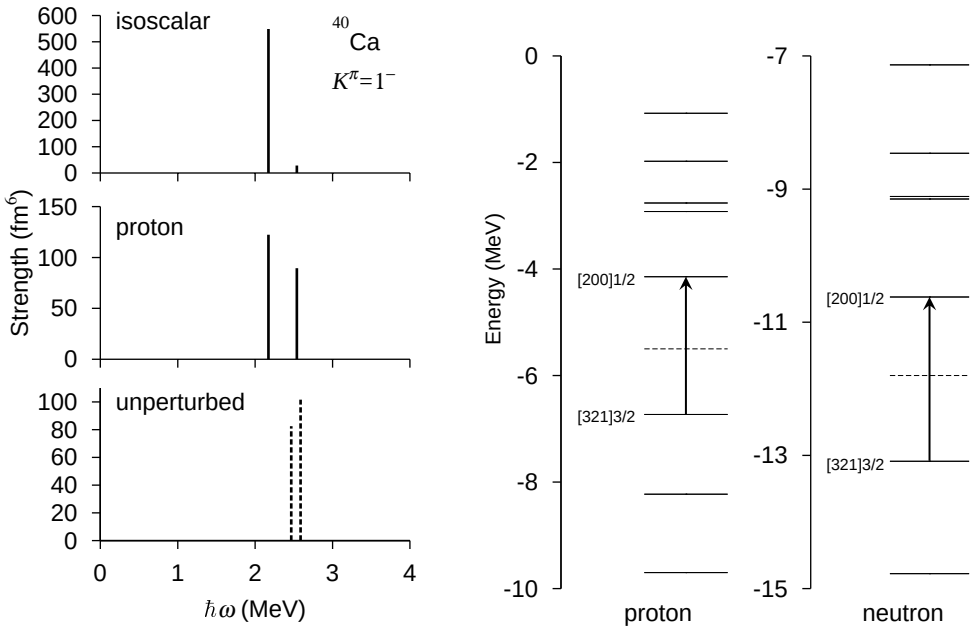

Fig. 3. *Left*: The isoscalar and proton octupole strengths, $B(Q^{\rm IS}3)$ and $B(E3)/e^2$, for the $K^\pi = 1^-$ excitations on the SD state in ^{40}Ca are plotted in the top and middle panels as functions of the excitation energy. These were obtained using an RPA calculation with $\beta_2 = 0.6$ for both protons and neutrons, using a box of size $\rho_{\max} \times z_{\max} = 8.25$ fm $\times 14.0$ fm. The unperturbed particle-hole strengths are also plotted with dashed lines in the bottom panel. *Right*: Particle-hole configurations generating the lowest $K^\pi = 1^-$ state at 2.2 MeV. The notation here is the same as in Fig. 2.

Table III. RPA amplitudes for the 1^- state 2.6 MeV in ^{36}S, calculated with $\beta_2 = 0.565$ and 0.685 for protons and neutrons, respectively. It is characterized by $B(E3) = 5.95$ e^2fm^6, $B(Q^\nu 3) = 189$ fm^6, $B(Q^{\rm IS}3) = 262$ fm^6, and $\sum |g_{ph}|^2 = 9.18 \times 10^{-3}$. Only components with $|f_{ph}| > 0.03$ are listed.

particle	hole	$\epsilon_p - \epsilon_h$(MeV)	f_{ph}	Q_{31}^{ph} (fm^3)	M_{31}^{ph} (fm^3)
ν[200]1/2	ν[321]3/2	2.71	−0.999	9.71	−10.5
ν[200]1/2	ν[330]1/2	6.11	−0.038	4.46	−0.22
π[200]1/2	π[330]1/2	5.23	−0.062	3.62	−0.28

Table IV. RPA amplitudes for the 2^- state 3.9 MeV in ^{36}S, calculated with $\beta_2 = 0.565$ and 0.685 for protons and neutrons, respectively. It is characterized by $B(E3) = 352$ e^2fm^6, $B(Q^\nu 3) = 97.0$ fm^6, $B(Q^{\rm IS}3) = 819$ fm^6, and $\sum |g_{ph}|^2 = 3.52 \times 10^{-2}$. Only components with $|f_{ph}| > 0.1$ are listed.

particle	hole	$\epsilon_p - \epsilon_h$(MeV)	f_{ph}	Q_{32}^{ph} (fm^3)	M_{32}^{ph} (fm^3)
ν[321]1/2	ν[202]5/2	4.75	−0.141	−8.37	1.34
ν[440]1/2	ν[321]3/2	5.19	0.137	6.34	1.01
ν[321]1/2	ν[211]3/2	11.7	−0.114	−12.5	1.85
π[321]3/2	π[211]1/2	4.45	−0.970	−12.5	14.2
π[321]1/2	π[211]3/2	12.9	−0.101	−10.8	1.43

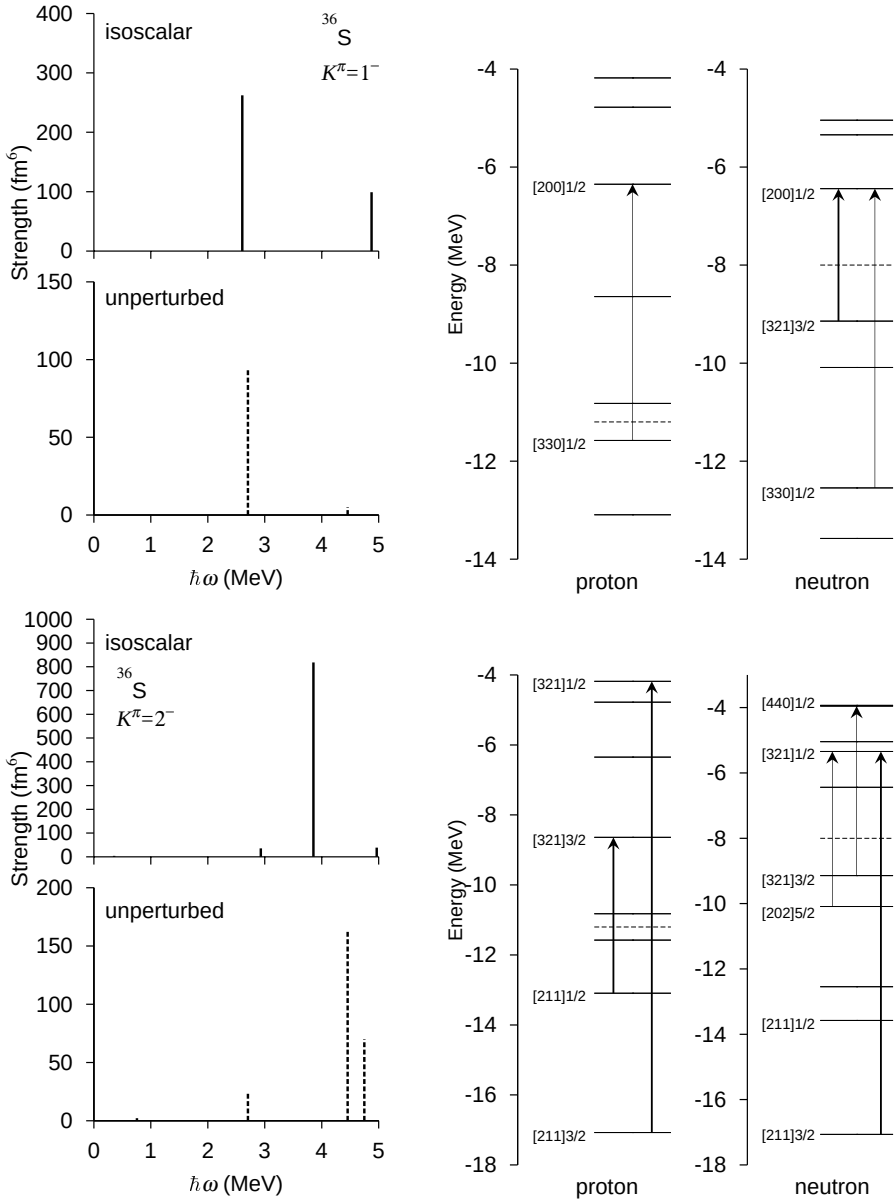

Fig. 4. *Upper left*: The isoscalar octupole strength $B(Q^{\rm IS}3)$ distribution for the $K^\pi = 1^-$ excitations on the SD state in ^{36}S is plotted in the top panel as a function of the excitation energy. This was obtained using an RPA calculation with $\beta_2 = 0.565$ and 0.685 for protons and neutrons, respectively, using a box of size $\rho_{\rm max} \times z_{\rm max} = 8.25$ fm $\times 14.0$ fm. The unperturbed particle-hole strength distribution is also plotted with dashed lines in the bottom panel. *Upper right*: Particle-hole configurations generating the lowest $K^\pi = 1^-$ state at 2.5 MeV. The notation is the same as in Fig. 2. *Lower left*: Same as above, but for the $K^\pi = 2^-$ excitations. *Lower right*: Same as above, but for the $K^\pi = 2^-$ excitation at 3.9 MeV.

$Z = 16$ and 20, respectively. It is thus interesting to consider the SD state in ^{36}S, which has $Z = 16$ and $N = 20$. Evidence for the existence of the SD band in this nucleus has been obtained from an SHF calculation.[39] The result of the RPA calculation is presented in Fig. 4, Table III and Table IV. There is a peak corresponding to $K^\pi = 1^-$ at 2.6 MeV with an isoscalar strength of about 3.4 W.u. and another peak corresponding to $K^\pi = 2^-$ at 3.9 MeV with an isoscalar strength of about 11 W.u. (1 W.u. $\simeq$ 77 fm^6 for ^{36}S). The $K^\pi = 1^-$ peak is associated with the particle-hole excitation from [321]3/2 to [200]1/2, while the $K^\pi = 2^-$ peak corresponds to the [211]1/2 $\rightarrow$ [321]3/2 excitation. These particle-hole configurations are the same as for the $K^\pi = 1^-$ state in ^{40}Ca and the $K^\pi = 2^-$ in ^{32}S discussed above. However, in contrast to the $N = Z$ nuclei, ^{32}S and ^{40}Ca, the coherence of proton and neutron excitations is absent in the case of ^{36}S. Thus, these RPA modes in ^{36}S are dominated by specific particle-hole configurations, although appreciable amounts of other particle-hole configurations collectively contribute to the $K^\pi = 2^-$ mode (see Table IV). The collectivity of these modes is apparently weak in comparison with the octupole vibrations built on the SD states in heavy nuclei,[48),49] because the number of particle-hole configurations contributing to the RPA modes is rather small in the nuclei under consideration. It should be mentioned, however, that transition strengths much larger than those in our results are obtained for these nuclei in the mixed representation RPA calculation carried out by Inakura et al.,[27),28] where no cutoff is imposed in the particle-hole excitation energy. The major cause of this difference may be the rather severe energy cutoff in the present RPA calculation. (See Ref. 50) for a numerical analysis of the contributions from very high-lying particle-hole configurations to the transition strengths of the low-lying RPA modes.)

3.2. *The SD state in ^{50}S*

In this subsection, we discuss the result for ^{50}S, which is, according to the SHF calculations,[39),46] close to the neutron drip line. The existence of the SD band in this nucleus is suggested in Ref. 39). The isoscalar octupole strength distribution with $K^\pi = 2^-$ calculated with the RPA is presented in Fig. 5. There are no peaks at any values of K in this energy region other than those corresponding to excitations to the discretized continuum. As we explain in detail below, the highest peak, at 3.1 MeV, with $K^\pi = 2^-$ is associated with the excitation of a single neutron from the loosely bound [310]1/2 state to the resonance [422]5/2 state. We obtain a peak of similar nature but with a smaller strength at 2.9 MeV. It is associated with the excitation

Table V. RPA amplitudes for the 2^- state at 3.1 MeV in ^{50}S, calculated with $\beta_2 = 0.54$ and 0.73 for protons and neutrons, respectively. It is characterized by $B(E3) = 19.4\ e^2\text{fm}^6$, $B(Q^\nu 3) = 5359$ fm^6, $B(Q^{\text{IS}}3) = 6023$ fm^6, and $\sum |g_{ph}|^2 = 6.42 \times 10^{-3}$. Only components with $|f_{ph}| > 0.1$ are listed.

particle	hole	$\epsilon_p - \epsilon_h$(MeV)	f_{ph}	Q_{32}^{ph} (fm^3)	M_{32}^{ph} (fm^3)
ν[303]7/2	ν[431]3/2	3.01	0.133	-11.6	-1.49
ν[422]5/2	ν[310]1/2	3.20	0.967	65.7	66.1
π[321]3/2	π[211]1/2	4.69	-0.138	-12.4	2.26

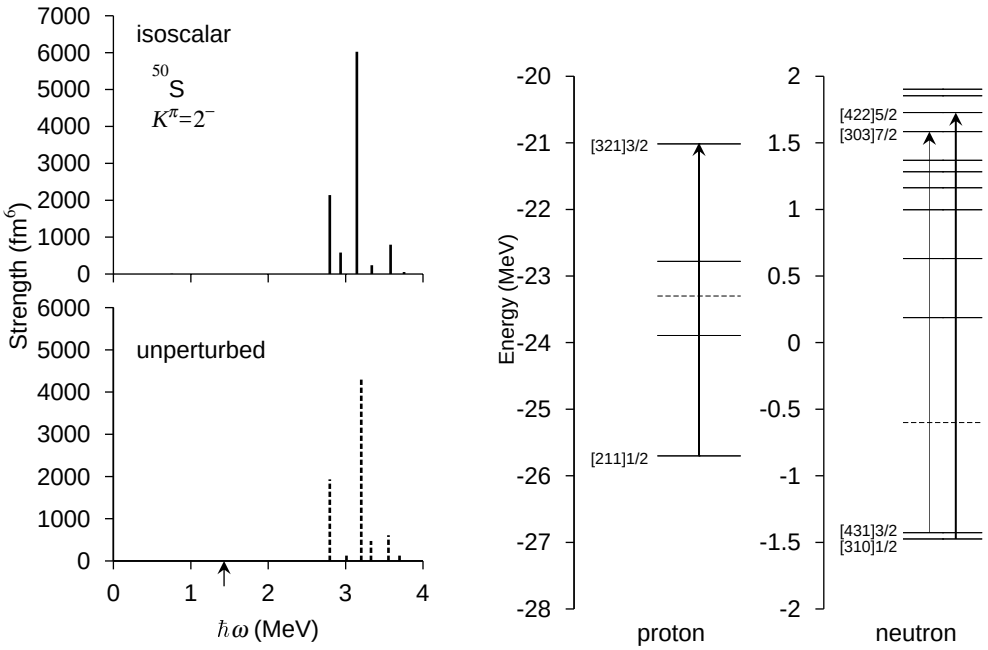

Fig. 5. *Left*: The isoscalar octupole strength $B(Q^{\rm IS}3)$ distribution for the $K^\pi = 2^-$ excitations built on the SD state in ^{50}S is plotted in the top panel as a function of the excitation energy. This was obtained using an RPA calculation with $\beta_2 = 0.54$ and 0.73 for protons and neutrons, respectively, using a box of size $\rho_{\rm max} \times z_{\rm max} = 14.25$ fm $\times 22.0$ fm. The unperturbed particle-hole strengths are also plotted with dashed lines in the bottom panel. The arrow indicates the threshold energy, $E_{\rm th} = 1.4$ MeV. *Right*: Particle-hole configurations generating the lowest $K^\pi = 2^-$ state at 3.1 MeV. The notation here is the same as in Fig. 2.

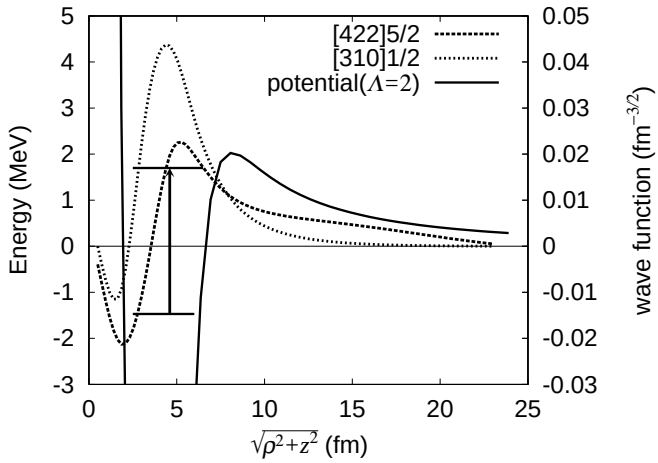

Fig. 6. The neutron particle-hole excitation contributing to the strongly enhanced transition strength of the $K^\pi = 2^-$ state at 3.1 MeV in superdeformed ^{50}S. The particle and hole states are labeled by their asymptotic quantum numbers. Their wave functions are plotted by the dotted curves. The solid curve denotes the neutron single-particle potential including the centrifugal barrier for $\Lambda = 2$. The horizontal axis represents $\sqrt{\rho^2 + z^2}$ along the $\theta = 45^\circ$ line.

of a single neutron from the loosely bound [431]3/2 state to the resonance [303]7/2 state. This difference in strength between the two peaks can be understood from the asymptotic selection rule (3·1c): The former particle-hole excitation satisfies it, whereas the latter does not. On the other hand, the second highest peak, at 2.8 MeV, is due to a neutron excitation from the [431]3/2 state to a discretized continuum state with $\Omega^\pi = 1/2^-$.

We now discuss the microscopic structure of the $K^\pi = 2^-$ excitation at 3.1 MeV in detail. It has an extremely strong isoscalar strength of $B(Q^{\rm IS}3) = 41$ W.u. and a weak electric strength of $B(E3) = 0.13$ W.u. (1 W.u. $\simeq 149$ fm^6 for ^{50}S). As shown in Table V, the major component of this RPA mode is the [310]1/2 $\rightarrow$ [422]5/2 excitation of a neutron. Their wave functions are plotted in Fig. 6. Because the [310]1/2 state is loosely bound and the [422]5/2 state is a resonance state, their wave functions extend significantly outside of the half-density radius of this nucleus. Together with the fact that this particle-hole configuration satisfies the asymptotic selection rule (3·1c), the very extended spatial structures of their wave functions are the main reason why it has the extremely large transition strength.

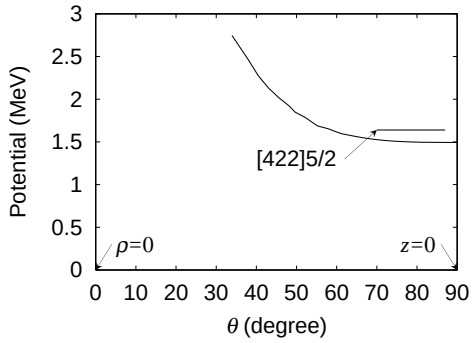

Fig. 7. Angle dependence of the centrifugal barrier height for the $\Lambda = 2$ states in superdeformed ^{50}S. The z- and ρ-axes correspond to $\theta = 0^\circ$ and 90°, respectively.

This [422]5/2 state has an interesting property: Because the centrifugal barrier is angle dependent, it lies below the barrier along the z-axis and 0.2 MeV above it along the ρ-axis (see Fig. 7). To determine whether or not the resonance interpretation of this state is valid, we first examined the box size dependence of calculated single-particle energies. As shown in Fig. 8, the energy of the [422]5/2 state is found to be stable with respect to variation of the box size. We next evaluated the sum of the eigenphase, $\Delta(E) = \sum_a \delta_a(E)$, following the procedure of Ref. 51). The eigenphase is obtained through eigenvalues of the S-matrix, and their sum has the same

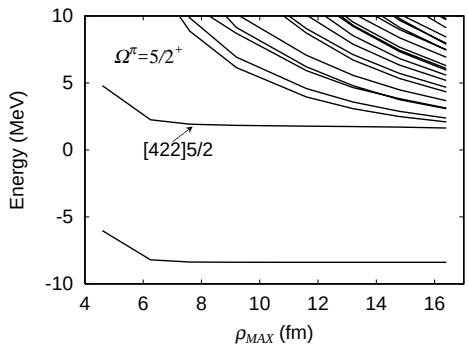

Fig. 8. Box size dependence of single-particle levels with $\Omega^\pi = 5/2^+$ in superdeformed ^{50}S. The [422]5/2 level is stable with respect to variation of the box size.

energy dependence around a resonance as the phase shift in a spherical system,[52]

$$\tan(\Delta(E) - \Delta_0(E)) = \frac{\Gamma}{2(E - E_R)}, \tag{3·2}$$

where E_R and Γ denote the resonance energy and the total width, respectively. The sum of the background eigenphases, $\Delta_0(E)$, is considered a slowly-varying quantity. The result of this calculation, presented in Fig. 9, confirms that the [422]5/2 state can be regarded as a resonance. Its width is estimated to be about 0.14 MeV. Furthermore, we confirmed that the root-mean-square radius of this state is clearly distinguishable from those of discretized continuum states (see Fig. 10). In this figure, the root-mean-square radius of various single-particle states are plotted. We find that not only the resonance [422]5/2 state but also the weakly bound [310]1/2 state has a root-mean-square radius about 2 fm larger than the average value for neutrons, $\sqrt{\langle r^2 \rangle}_\nu = 4.44$ fm. This is because the low angular momentum $p_{1/2}$ component that has a spatially extended structure becomes dominant in such a $\Omega^\pi = 1/2^-$ neutron level as the binding energy approaches zero.[53),54)]

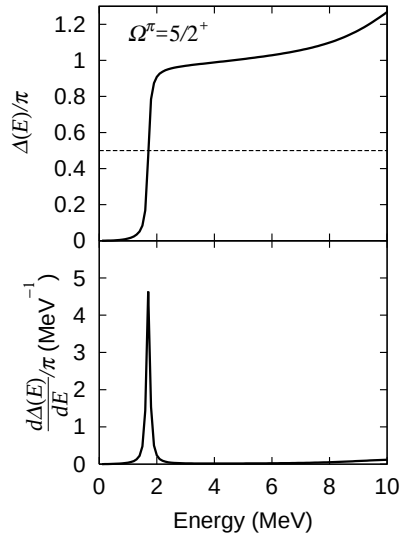

Fig. 9. The eigenphase sum (upper panel) and its derivative (lower panel) for the $\Omega^\pi = 5/2^+$ state in superdeformed ^{50}S are plotted as functions of energy.

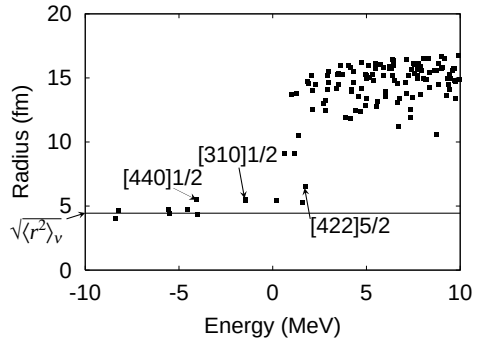

Fig. 10. Root-mean-square radii $\sqrt{\langle r^2 \rangle}$ of neutron single-particle states in superdeformed ^{50}S, obtained in a calculation using a box of size $\rho_{\max} \times z_{\max} = 14.25$ fm $\times$ 22.0 fm. Here, the root-mean-square radius of neutrons $\sqrt{\langle r^2 \rangle_\nu}$ is 4.44 fm.

In contrast to the peak at 3.1 MeV discussed above, the peak at 2.8 MeV corresponds to the excitation of the loosely bound [431]3/2 neutron to a discretized continuum state with $\Omega^\pi = 1/2^-$. Therefore, its position and height do not have definite physical meanings. In fact, these values change as the box size is varied. This peak even disappears when smaller boxes are used in the numerical calculation (see Fig. 11), whereas the peak position and the height associated with the [310]1/2 $\rightarrow$ [422]5/2 excitation is stable, as long as a box larger than $\rho_{\max} \times z_{\max} = 12.25$ fm $\times 20.0$ fm is used. We should also mention

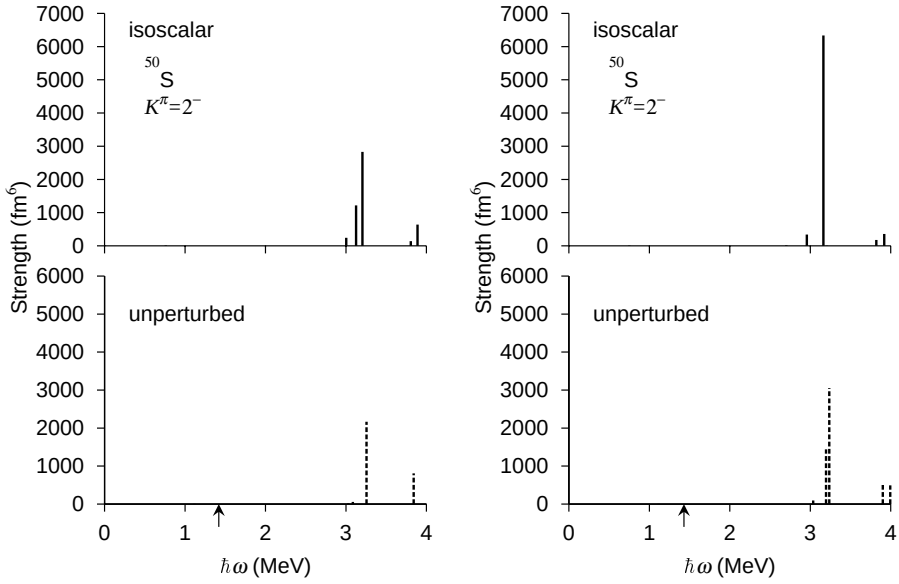

Fig. 11. The isoscalar octupole strength $B(Q^{\rm IS}3)$ distributions for the $K^\pi = 2^-$ excitations on the SD state in ^{50}S, obtained using an RPA calculation with $\beta_2 = 0.54$ and 0.73 for protons and neutrons, respectively, using a box of size $\rho_{\rm max} \times z_{\rm max} = 10.25$ fm $\times 16.0$ fm (left) and 12.25 fm $\times 20.0$ fm (right). The neutron root-mean-square radii $\sqrt{\langle r^2 \rangle_\nu}$ are 4.42 fm and 4.44 fm. The unperturbed particle-hole strengths are also plotted with dashed lines in the bottom panels. The arrows indicate the threshold energy, $E_{\rm th} = 1.4$ MeV.

that the convergence of the numerical calculation is insufficient for the unperturbed strength of the $[310]1/2 \rightarrow [422]5/2$ transition, because the root-mean-square radius of the $[422]5/2$ state still increases from 5.90 fm to 6.54 fm for a larger box, with $\rho_{\rm max} \times z_{\rm max} = 14.25$ fm $\times 22.0$ fm. Therefore, the calculated transition strength has only qualitative meaning.

Finally, let us make a comparison between the spatial distributions of the $K^\pi = 2^-$ octupole strength associated with individual particle-hole excitations on the SD state in the drip line nucleus ^{50}S and those in the stable nucleus ^{32}S. Figure 12 plots the spatial distribution functions $Q^{ph}_{3K}(\rho, z)$ for some major configurations generating the low-lying $K^\pi = 2^-$ modes in ^{32}S and ^{50}S. It is clear that the particle-hole excitations in ^{50}S have spatial distributions significantly extended outside of the nucleus, while those in ^{32}S are peaked around the surface region. This spatially extended structure brings about a strong enhancement of the octupole strength in ^{50}S. This can be regarded as one of the unique properties of excitation modes in nuclei close to the drip line. Note that this mechanism of transition strength enhancement is different from the threshold effect associated with the excitation of a loosely bound neutron into the non-resonant continuum.[55)]

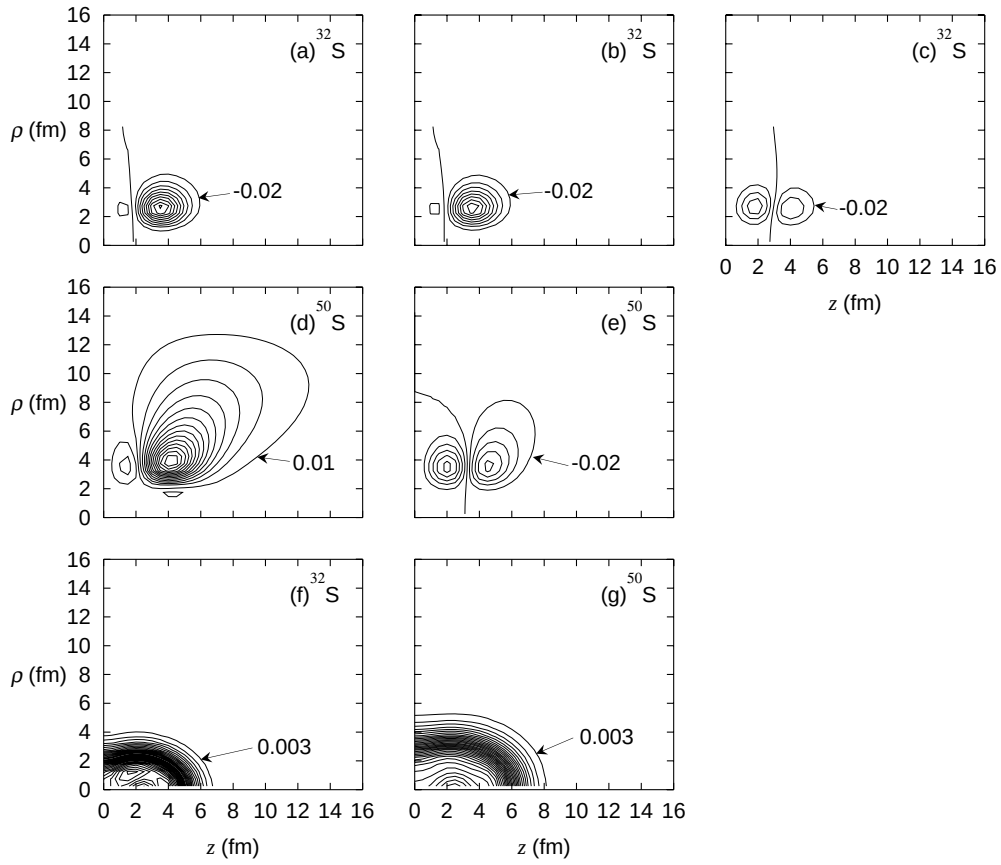

Fig. 12. Spatial distribution functions $Q_{32}^{ph}(\rho, z)$ for some particle-hole excitations generating the low-lying $K^\pi = 2^-$ states in superdeformed ^{32}S and ^{50}S. The contour lines are plotted at intervals of 0.02 fm. The panels denoted (a), (b) and (c) correspond to the $[211]1/2 \rightarrow [321]3/2$, $[211]3/2 \rightarrow [321]1/2$, and $[330]1/2 \rightarrow [202]5/2$ excitations in ^{32}S, respectively, while (d) and (e) correspond to the $[310]1/2 \rightarrow [422]5/2$ and $[431]3/2 \rightarrow [303]7/2$ excitations in ^{50}S. The bottom panels, (f) and (g), display the neutron density distributions of the SD states in ^{32}S and ^{50}S, respectively. The contour lines are plotted at intervals of 0.003 fm^{-3}. The neutron root-mean-square radii, $\sqrt{\langle r^2 \rangle_\nu}$, are 3.49 and 4.44 fm for ^{32}S and ^{50}S, respectively.

3.3. *The oblately deformed state in ^{40}Mg*

To show that the strong enhancement of the transition strength for an excitation from a loosely bound state to a resonance state is not restricted to the SD states but expected to be a rather general phenomenon in nuclei close to the drip line, we present in this subsection another example of the RPA calculation for ^{40}Mg. According to the HF-Bogoliubov calculations,[56),57)] this nucleus is situated close to the neutron drip line and possesses both prolate and oblate local minima.

Figure 13 displays the octupole transition strengths for the $K^\pi = 3^-$ excita-

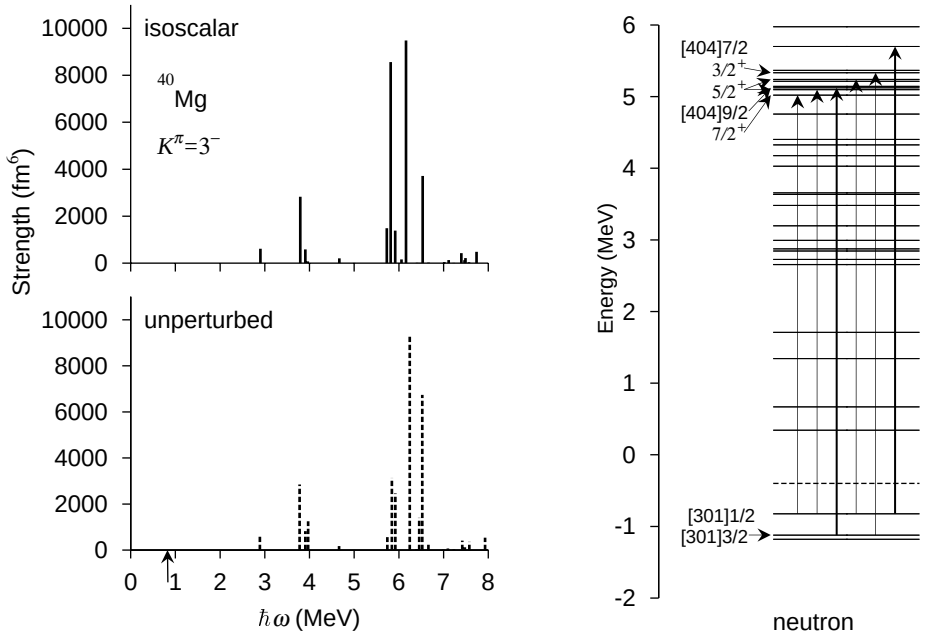

Fig. 13. *Left*: The isoscalar octupole strength $B(Q^{\rm IS}3)$ distribution for the $K^\pi = 3^-$ excitations on the oblate state in ^{40}Mg is plotted in the top panel as a function of the excitation energy. This was obtained using an RPA calculation with $\beta_2 = -0.2$ for both protons and neutrons, using a box of size $\rho_{\max} \times z_{\max} = 14.25$ fm $\times 12.0$ fm. The unperturbed particle-hole strengths are also plotted with dashed lines in the bottom panel. The arrow indicates the threshold energy $E_{\rm th} = 0.82$ MeV. *Right*: Particle-hole configurations of neutrons generating the $K^\pi = 3^-$ state at 6.2 MeV. The levels denoted [404]9/2 and [404]7/2 correspond to resonances, while other levels in the positive energy region represent discretized continuum states.

Table VI. RPA amplitudes for the 3^- state at 6.2 MeV in the oblately deformed ^{40}Mg, calculated with $\beta_2 = -0.2$ for both protons and neutrons. It is characterized by $B(E3) = 1.09\ e^2{\rm fm}^6$, $B(Q^\nu 3) = 9280$ fm^6, $B(Q^{\rm IS}3) = 9482$ fm^6, and $\sum |g_{ph}|^2 = 1.46 \times 10^{-3}$. The particle states other than the ν[404]9/2 and ν[404]7/2 resonances represent discretized continuum states. Only components with $|f_{ph}| > 0.1$ are listed.

particle	hole	$\epsilon_p - \epsilon_h$(MeV)	f_{ph}	Q^{ph}_{33} (fm^3)	M^{ph}_{33} (fm^3)
ν 7/2$^+$	ν[301]1/2	5.84	−0.142	−56.0	7.81
ν 5/2$^+$	ν[301]1/2	5.92	0.156	49.6	7.58
ν 5/2$^+$	ν[301]1/2	6.06	0.211	−0.526	−0.109
ν[404]9/2	ν[301]3/2	6.24	0.909	−96.7	−89.5
ν 3/2$^+$	ν[301]3/2	6.45	0.171	−37.4	−6.51
ν[404]7/2	ν[301]1/2	6.52	0.160	−82.1	−13.3

tions on the oblately deformed state in ^{40}Mg. Among several peaks in the isoscalar strength distribution, we can give a clear physical interpretation for the two prominent peaks at 6.2 and 6.6 MeV: The former is created by the excitation of a neutron from the loosely bound [301]3/2 state to the resonance [404]9/2 state, while the latter is from the loosely bound [301]3/2 state to the resonance [404]7/2 state. These

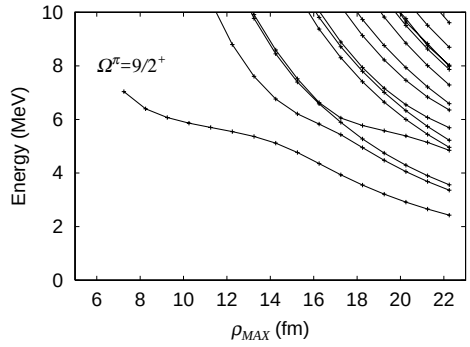

Fig. 14. Box size dependence of single-particle levels with $\Omega^\pi = 9/2^+$ in the oblately deformed ^{40}Mg.

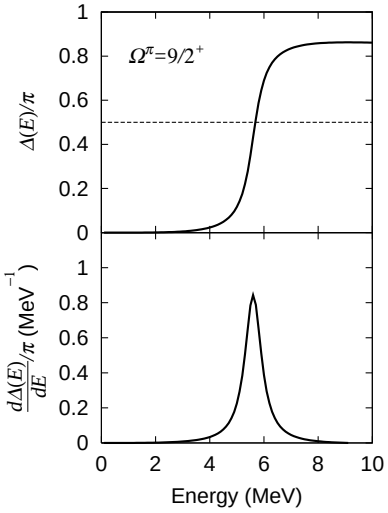

Fig. 15. The eigenphase sum (upper panel) and its derivative (lower panel) for the $\Omega^\pi = 9/2^+$ state in the oblately deformed ^{40}Mg are plotted as functions of energy.

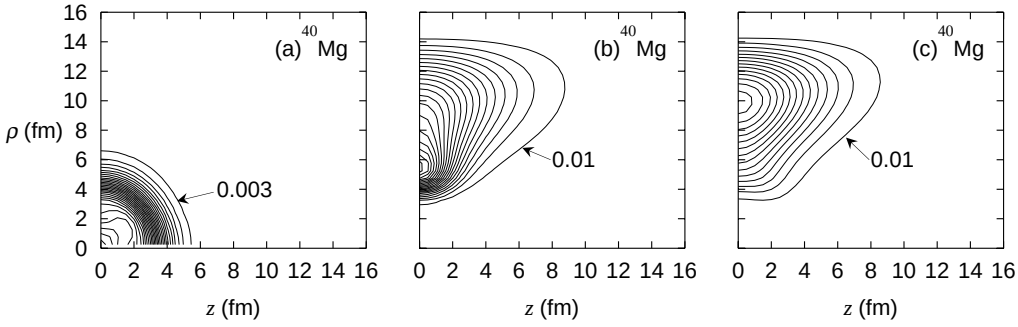

Fig. 16. (a) The neutron density distribution of the oblately deformed state in ^{40}Mg. The contour lines are plotted at intervals of 0.003 fm^{-3}. The root-mean-square radius of neutrons, $\sqrt{\langle r^2\rangle_\nu}$, is 4.06 fm. (b) Spatial distribution function $Q_{33}^{ph}(\rho, z)$ for the [301]3/2 $\rightarrow$ [404]9/2 excitation on the oblately deformed state in ^{40}Mg. The contour lines are plotted at intervals of 0.02 fm. (c) Same as (b), but for the [301]1/2 $\rightarrow$ [404]7/2 excitation.

resonance states are associated with the $g_{9/2}$ orbit, which has a high centrifugal barrier. Due to the spatially extended structure of this type of particle-hole excitation, they acquire extremely large transition strengths; the isoscalar octupole strength of the former (latter) is about 90 (39) W.u. (1 W.u. $\simeq$ 95 fm^6 for ^{40}Mg). The major components of the RPA amplitudes of the $K^\pi = 3^-$ mode at 6.2 MeV are presented in Table VI. Other peaks in this figure are due to excitations to discretized continuum states; e.g., the peak at 3.8 (5.8) MeV is associated with the excitation from the [301]3/2 ([301]1/2) state to the discretized continuum Ω^π=3/2$^+$ (7/2$^+$)

state. Therefore, their positions and peak heights do not have definite physical meanings. This conclusion was obtained by examining the box size dependence of single-particle energies and their eigenphase sums. Typical results of these calculations are presented in Figs. 14 and 15. The widths of the resonant [404]9/2 and [404]7/2 states are estimated to be about 0.8 and 1.2 MeV, respectively.

Finally, we show in Fig. 16 the spatial distribution functions $Q_{33}^{ph}(\rho, z)$ for the $[301]3/2 \rightarrow [404]9/2$ and $[301]1/2 \rightarrow [404]7/2$ excitations, together with the neutron density distribution of the oblately deformed state in ^{40}Mg. It is clearly seen that the strengths of these particle-hole excitations extend far from the nuclear surface. Furthermore, we notice that the peak positions of the two distributions, shown in (b) and (c), differ considerably. This can be regarded as the major reason that the two particle-hole configurations do not strongly mix with each other in the RPA eigenmodes, despite the fact that their unperturbed energies are fairy close (see Table VI). This is quite different from the familiar situations for low-frequency RPA modes in stable nuclei, in which the strength distribution functions of many particle-hole configurations have peaks near the nuclear surface and tend to mix with each other, generating collective vibrational modes.

§4. Conclusions

By means of the RPA calculation based on the deformed Woods-Saxon potential in the coordinate-mesh representation, we have carried out a comparative study of octupole excitations built on the SD states in the ^{40}Ca region and those in ^{50}S. In the $N = Z$ stable nuclei, ^{32}S and ^{40}Ca, the enhancement of the octupole transition strength results from the coherence between the proton and neutron excitations. By contrast, in ^{50}S close to the neutron drip line, we have found that the low-lying state created by the excitation of a single neutron from a loosely bound low Ω state to a high Ω resonance state acquires an extremely large transition strength. We have made a detailed study of the spatial distributions of particle-hole transition strengths and confirmed that this enhancement of the strength is a natural consequence of the fact that these particle and hole wave functions extend significantly outside of the nuclear surface. To show that this kind of enhancement phenomenon is not restricted to the SD states, we have also presented another example for oblately deformed ^{40}Mg close to the neutron drip line.

The present calculation indicates that, as we approach the drip line, it becomes increasingly difficult to generate collective modes of excitation by coherent superpositions of many particle-hole excitations. This is because the bound particle states disappear and individual resonance wave functions possess different spatial structures. It should be emphasized, however, that the pairing correlation is not taken into account in the present calculation. Quite recently, one of the authors (M. Y.) showed[58] that collectivity emerges in nuclei close to the drip line, owing to the pairing anti-halo effect:[59] The self-consistent pairing correlation in the continuum brings about spatial localization of particle-hole excitations, which helps in generating the collective modes of excitation. Thus, it is an important next step to investigate how

the results presented in this paper are modified by the pairing correlation.

Acknowledgements

We thank S. Mizutori and T. Inakura for valuable discussions and comments. We are grateful to K. Hagino for useful suggestions and for providing us with a computer program for calculation of the eigenphase sum. This work was done as a step in our long-range plan to explore exotic modes of excitation unique in deformed nuclei close to the drip line, and it is supported by the Japan-U.S. Cooperative Science Program "Mean-Field Approach to Collective Excitations in Unstable Medium-Mass and Heavy Nuclei", a Grant-in-Aid for the 21st Century COE "Center for Diversity and Universality in Physics" from the Ministry of Education, Culture, Sports, Science and Technology (MEXT) of Japan, and a Grant-in-Aid for Scientific Research No. 16540249 from the Japan Society for the Promotion of Science. The numerical calculations were performed on the NEC SX-5 supercomputer at Yukawa Institute for Theoretical Physics, Kyoto University.

Appendix A
—— Numerical Derivative ——

For wave functions of the form $\Phi(\rho,\varphi,z)=\phi(\rho,z)e^{i\Lambda\varphi}$, we have

$$\nabla^2\phi(\rho,z)e^{i\Lambda\varphi}=\left(\frac{1}{\rho}\frac{\partial}{\partial\rho}+\frac{\partial^2}{\partial\rho^2}-\frac{\Lambda^2}{\rho^2}+\frac{\partial^2}{\partial z^2}\right)\phi(\rho,z)e^{i\Lambda\varphi}. \tag{A·1}$$

Using the coordinate-mesh representation and the 9-points formula, the derivative parts can be written as

$$\begin{aligned}
&\left(\frac{1}{\rho}\frac{\partial}{\partial\rho}+\frac{\partial^2}{\partial\rho^2}+\frac{\partial^2}{\partial z^2}\right)\phi_{i,j}\\
&=\frac{1}{\Delta^2}\left[\frac{287000}{5040}\phi_{i,j}+\left(\frac{8064}{5040}+\frac{672}{840(i-1/2)}\right)\phi_{i+1,j}+\left(\frac{8064}{5040}-\frac{672}{840(i-1/2)}\right)\phi_{i-1,j}\right.\\
&\quad-\left(\frac{1008}{5040}+\frac{168}{840(i-1/2)}\right)\phi_{i+2,j}-\left(\frac{1008}{5040}-\frac{168}{840(i-1/2)}\right)\phi_{i-2,j}\\
&\quad+\left(\frac{128}{5040}+\frac{32}{840(i-1/2)}\right)\phi_{i+3,j}+\left(\frac{128}{5040}-\frac{32}{840(i-1/2)}\right)\phi_{i-3,j}\\
&\quad-\left(\frac{9}{5040}+\frac{3}{840(i-1/2)}\right)\phi_{i+4,j}-\left(\frac{9}{5040}-\frac{3}{840(i-1/2)}\right)\phi_{i-4,j}\\
&\qquad+\frac{8064}{5040}(\phi_{i,j+1}+\phi_{i,j-1})-\frac{1008}{5040}(\phi_{i,j+2}+\phi_{i,j-2})\\
&\qquad\left.+\frac{128}{5040}(\phi_{i,j+3}+\phi_{i,j-3})-\frac{9}{5040}(\phi_{i,j+4}+\phi_{i,j-4})\right].
\end{aligned} \tag{A·2}$$

Appendix B
Numerical Quadrature

For numerical integration, we use Bode's rule given by

$$\int_{x_i}^{x_{i+4}} f(x)dx = \frac{2\Delta}{45}(7f_i + 32f_{i+1} + 12f_{i+2} + 32f_{i+3} + 7f_{i+4}) + O(\Delta^7). \qquad \text{(B·1)}$$

This formula is a generalization of the well-known Simpson's rule, and it is derived by taking into account polynomials up to quartic order in the Taylor expansion for interpolation between the mesh points.[60)]

References

1) Ed. I. Tanihata, Nucl. Phys. A **693** (2001), Issues 1, 2.
2) Ed. H. Horiuchi, T. Otsuka and Y. Suzuki, Prog. Theor. Phys. Suppl. No. 142 (2001).
3) Ed. K. Hagino, H. Horiuchi, M. Matsuo and I. Tanihata, Prog. Theor. Phys. Suppl. No. 146 (2002).
4) I. Hamamoto, H. Sagawa and X. Z. Zhang, Phys. Rev. C **53** (1996), 765; ibid. **55** (1997), 2361; ibid. **56** (1997), 3121; ibid. **57** (1998), R1064; ibid. **64** (2001), 024313.
5) I. Hamamoto and H. Sagawa, Phys. Rev. C **60** (1999), 064314; ibid. **62** (2000), 024319; ibid. **66** (2002), 044315.
6) S. Shlomo and B. Agrawal, Nucl. Phys. A **722** (2003), C98.
7) K. Hagino and H. Sagawa, Nucl. Phys. A **695** (2001), 82.
8) M. Bender, J. Dobaczewski, J. Engel and W. Nazarewicz, Phys. Rev. C **65** (2002), 054322.
9) M. Yamagami and Nguyen Van Giai, Phys. Rev. C **69** (2004), 034301.
10) J. Terasaki, J. Engel, M. Bender, J. Dobaczewski, W. Nazarewicz and M. Stoitsov, nucl-th/0407111.
11) D. Vretenar, T. Nikšić, N. Paar and P. Ring, Nucl. Phys. A **731** (2004), 281.
12) N. Paar, P. Ring, T. Nikšić and D. Vretenar, Phys. Rev. C **67** (2003), 034312.
13) N. Paar, T. Nikšić, D. Vretenar and P. Ring, Phys. Rev. C **69** (2004), 054303.
14) G. Giambrone, S. Scheit, F. Barranco, P. F. Bortignon, G. Colò, D. Sarchi and E. Vigezzi, Nucl. Phys. A **726** (2003), 3.
15) M. Bender, P.-H. Heenen and P.-G. Reinhard, Rev. Mod. Phys. **75** (2003) 121.
16) S. Shlomo and G. F. Bertsch, Nucl. Phys. A **243** (1975), 507.
17) G. F. Bertsch and S. F. Tsai, Phys. Rep. **18** (1975), 125.
18) M. Matsuo, Nucl. Phys. A **696** (2001), 371.
19) M. Matsuo, Prog. Theor. Phys. Suppl. No. 146 (2002), 110.
20) M. Matsuo, K. Mizuyama and Y. Serizawa, nucl-th/0408052.
21) E. Khan, N. Sandulescu, M. Grasso and N. V. Giai, Phys. Rev. C **66** (2002), 024309.
22) E. Khan, N. Sandulescu, N. V. Giai and M. Grasso, Phys. Rev. C **69** (2004), 014314.
23) P. Urkedal, X. Z. Zhang and I. Hamamoto, Phys. Rev. C **64** (2001), 054304.
24) T. Nakatsukasa and K. Yabana, *Proc. Int. Symp. "A New Era of Nuclear Structure Physics", Niigata 2003*, ed. Y. Suzuki, S. Ohta, M. Matsuo and T. Ohtsubo (Word Scientific, 2004), p. 251.
25) T. Nakatsukasa and K. Yabana, Phys. Rev. C **71** (2005), 024301.
26) K. Hagino, Nguyen Van Giai and H. Sagawa, Nucl. Phys. A **731** (2004), 264.
27) T. Inakura, M. Yamagami, K. Matsuyanagi, S. Mizutori, H. Imagawa and Y. Hashimoto, *Proc. the 10th Marie and Pierre Curie Nuclear Physics Workshop, 24-28 September, 2003, Kazimierz Dolny, Poland*, Int. J. Mod. Phys. E **13** (2004), 157.
28) T. Inakura, Doctor Thesis (Kyoto University, 2004).
29) R. H. Lemmer and M. Véneroni, Phys. Rev. **170** (1968), 883.
30) A. Muta, J.-I. Iwata, Y. Hashimoto and K. Yabana, Prog. Theor. Phys. **108** (2002), 1065.
31) H. Imagawa and Y. Hashimoto, Phys. Rev. C **67** (2003), 037302.
32) H. Imagawa, Doctor Thesis, University of Tsukuba (2003).
33) E. Ideguchi et al., Phys. Rev. Lett. **87** (2001), 222501.
34) C. J. Chiara et al., Phys. Rev. C **67** (2003), 041303(R).

35) H. C. Pauli, Phys. Rep. **7** (1973), 35.
36) A. Bohr and B. R. Motteleson, *Nuclear Structure*, vol. I (Benjamin, 1969).
37) S. Cwiok, J. Dudek, W. Nazarewicz, J. Skalski and T. Werner, Comput. Phys. Commun. **46** (1987), 379.
38) P. Ring and P. Schuck, *The Nuclear Many-Body Problem* (Springer, 1980).
39) T. Inakura, M. Yamagami, S. Mizutori and K. Matsuyanagi, Nucl. Phys. A **728** (2003), 52.
40) I. Ragnarsson, S. G. Nilsson and R. K. Sheline, Phys. Rep. **45** (1978), 1.
41) J. Dobaczewski, AIP Conf. Proc. **481** (1999), 315.
42) M. Yamagami and K. Matsuyanagi, Nucl. Phys. A **672** (2000), 123.
43) H. Molique, J. Dobaczewski and J. Dudek, Phys. Rev. C **61** (2000), 044304.
44) R. R. Rodriguez-Guzmán, J. L. Egido and L. M Robeldo, Phys. Rev. C **62** (2000), 054308.
45) T. Tanaka, R. G. Nazmitdinov and K. Iwasawa, Phys. Rev. C **63** (2001), 034309.
46) T. R. Werner, J. A. Sheikh, M. Misu, W. Nazarewicz, J. Rikovska, K. Heeger, A. S. Umar and M. R. Strayer, Nucl. Phys. A **597** (1996), 327.
47) S. Mizutori, T. Nakatsukasa, K. Arita, Y. R. Shimizu and K. Matsuyanagi, Nucl. Phys. A **557** (1993), 125.
48) T. Nakatsukasa, K. Matsuyanagi, S. Mizutori and Y. R. Shimizu, Phys. Rev. C **53** (1996), 2213.
49) T. Nakatsukasa, K. Matsuyanagi, S. Mizutori and W. Nazarewicz, Phys. Lett. B **343** (1995), 19.
50) J. P. Blaizot and D. Gogny, Nucl. Phys. A **284** (1977), 429.
51) K. Hagino and Nguyen Van Giai, Nucl. Phys. A **735** (2004), 55.
52) A. U. Hazi, Phys. Rev. A **19** (1979), 920.
53) T. Misu, W. Nazarewicz and S. Åberg, Nucl. Phys. A **614** (1997), 44.
54) I. Hamamoto, Phys. Rev. C **69** (2004), 041306.
55) F. Catara, E. G. Lanza, M. A. Nagarajan and A. Vitturi, Nucl. Phys. A **624** (1997), 449.
56) J. Terasaki, H. Flocard, P.-H. Heenen and P. Bonche, Nucl. Phys. A **621** (1997), 706.
57) M. V. Stoitsov, J. Dobaczewski, W. Nazarewicz, S. Pittel and D. J. Dean, Phys. Rev. C **68** (2003), 054312.
58) M. Yamagami, *Proceedings of the Fifth Japan China Joint Nuclear Physics Symposium, 7-10 March, 2004, Kyushu University, Japan*; nucl-th/0404030.
59) K. Bennaceur, J. Dobaczewski and M. Ploszajczak, Phys. Lett. B **496** (2000), 154.
60) S. E. Koonin, *Computational Physics* (Addison-Wesley, 1986).